molecular pharmaceutics

ARTICLE

pubs.acs.org/molecularpharmaceutics

Iodine-124 as a Label for Pharmacological PET Imaging

Vasily V. Belov,[†,‡,§] Ali A. Bonab,[†,‡,§] Alan J. Fischman,[‡,§] Michael Heartlein,[∥] Pericles Calias,[∥] and Mikhail I. Papisov[*,†,‡,§]

[†]Department of Radiology, Massachusetts General Hospital, Boston, Massachusetts

[‡]Harvard Medical School, Boston, Massachusetts

[§]Shriners Burns Hospital—Boston, Boston, Massachusetts

[∥]Shire Human Genetic Therapy, Lexington, Massachusetts

ABSTRACT: With the growing number of biotechnology products and drug delivery systems entering preclinical and clinical studies, pharmacological imaging studies with PET play an increasingly significant role. Such studies often require investigation of slow and complex pharmacokinetics (PK). This suggests labeling of the drug candidate with radionuclides that have long physical half-lives. Among the currently available PET positron emitters, ^{124}I has the longest physical half-life (4.2 days). This, combined with the well-investigated behavior of iodine in vivo, makes ^{124}I very attractive for pharmacological studies. However, the high energy of the positrons emitted by ^{124}I and the presence of single photons in the ^{124}I emission can potentially introduce limitations in the quantitative analysis of the images. The objective of this research was to determine whether the use of ^{124}I as a PET label provides data quality suitable for PK studies. The study was carried out using MicroPET P4 scanner (Siemens/Concorde Microsystems). Spatial resolution, count-rate performance, sensitivity and scatter fraction were measured using a line source and a cylindrical phantom. Model animal studies in rats and cynomolgus monkeys were carried out using human recombinant proteins. The proteins were labeled with ^{124}I, up to 185 MBq/mg. The transaxial and axial spatial resolutions in the center of the camera were satisfactory and higher for OSEM3D/MAP than FORE-2DFBP (FWHM 2.52 vs 3.31 mm, and 3.10 vs 3.69 mm). Linearity of the true coincidence count-rate was observed up to 44 MBq. Animal studies demonstrated excellent delineation and resolution of even very small organs. At optimal doses, 2−10 MBq per animal for rodents and 4−10 MBq per kg of body weight for larger animals, the quality of numerical data was appropriate for PK analysis in all experimental timeframes from minutes (dynamic studies) to 10 days. Overall, the data suggest that ^{124}I is an excellent label for quantitative pharmacological PET imaging studies.

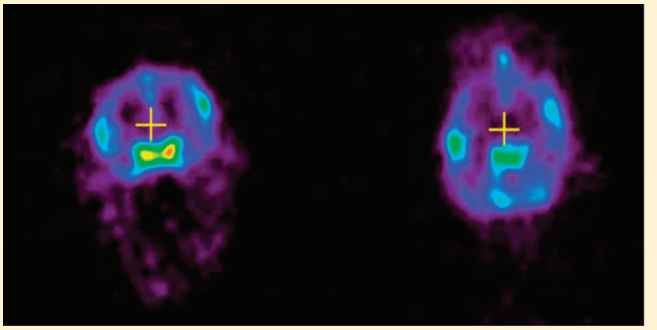

KEYWORDS: Iodine-124, Positron Emission Tomography, Pharmacology, Pharmacokinetics, Biopharmaceuticals, Macromolecules

INTRODUCTION

With the growing number of drug delivery systems and "large molecule" drugs, the action of which relies on nontrivial pharmacokinetics, quantitative imaging will play an increasingly significant role in both preclinical and human studies.

PET is a powerful tool for quantitative in vivo tracking of molecules labeled with positron-emitting radionuclides. The high sensitivity, format and accuracy of data similar to those of conventional tissue-sampling biodistribution studies make PET a readily adoptable pharmacological technique. In contrast to the conventional studies, PET also allows for longitudinal nonterminal same-animal studies. The latter may not only improve the data statistics but also enable preclinical studies (especially in large and/or rare animals) not feasible under the conventional approach.

Considering the commercial availability of PET scanners specifically designed for animal studies,[1−7] the spatial resolution of which is sufficient for delineating the organs and structures of interest in animals (from rodents to nonhuman primates), feasibility of a particular PET study mainly depends on the availability of a radionuclide suitable for such study. In the pharmacokinetics research, the data are usually needed for multiple time points over a period of up to several days, depending on the rates of the physiological processes being studied. Thus, the radionuclide should have a physical half-life long enough to cover the entire length of the study. In addition, the interpretability of the late stage data influenced by metabolization of the labeled substance depends on the knowledge on the label behavior in vivo.

Among the currently available positron emitters suitable for imaging with PET, ^{124}I has the longest physical half-life of 4.2

Received: October 19, 2010
Accepted: March 1, 2011
Revised: February 11, 2011
Published: March 01, 2011

days. Combined with the well-investigated behavior of iodine as a label in vivo (in numerous studies utilizing ^{123}I, ^{125}I and ^{131}I), this makes ^{124}I a very appealing label for quantitative pharmacokinetics studies.

However, two major features of the radioactive decay of ^{124}I have to be accounted for. One is the high energy and therefore long range of the emitted positrons, which can be expected to limit the image resolution. The other is a high fraction of non-positron decays accompanied by single photon emission in the same energy window with the annihilation photons: 60.5% of all decays result in a 602 keV photon, and half of the positron-producing decays contain such photon in the same cascade. If not taken into account, these factors may lead to significant degradation of spatial resolution, sensitivity, and signal linearity, and also to elevated background caused by the higher scatter and randoms events than for "pure" positron emitters such as, for example, ^{18}F. This would not only impair the image quality but also make the numerical data obtained from the images hardly quantitative. The contemporary PET scanners have well developed hardware and software, in which various means of data correction for system dead-time, randoms and scatter events are implemented. The appropriate use of these tools (within certain limits) can alleviate the above problem. Previous studies[8−14] assessed the impact of ^{124}I decay characteristics on clinical PET imaging, where image reconstruction is optimized for clinical diagnostic applications and the (intrinsically low) image resolution is not expected to be as affected by the positron energy as in higher resolution preclinical systems.

The present study was aimed to determine whether and within what limits the properties of ^{124}I as a positron emitter can translate into data quality suitable for pharmacological research utilizing a preclinical PET scanner.

EXPERIMENTAL SECTION

Scanner Description and System Settings. The study was carried out using MicroPET P4 scanner (Siemens/CTI Concorde Microsystems, TN).[2] This imager was designed for small primate studies (opening 22 cm, axial field of view 7.89 cm, transaxial field of view 19 cm). Imagers of MicroPET family has been used in numerous studies, and the P4 model (along with its successor, Focus 220) is most widely used in small primate research.

The MicroPET P4 detection system is composed of 168 fast lutetium oxyorthosilicate (LSO) based block detectors arranged in four detector rings that are 26 cm in diameter. Each block of LSO (19 × 19 × 10 mm^3) is cut into an 8 × 8 array of scintillation crystals that are 2.1 mm (axial) × 2.1 mm (transaxial) × 10 mm (deep). The LSO array is coupled through a 10 cm multiclad fiber optic bundle to position sensitive Hamamatsu R5900-C8 photomultiplier tubes.

The imager works in 3D mode without interplane septa, acquiring data in list-mode by a host PC running Windows XP (Microsoft, WA) through an optic fiber link. Before the reconstruction, the emission list-mode data were histogrammed into a total of 1024 3D sinograms by grouping together three adjacent lines of response (LORs) having a crystal ring difference of up to 31.

By interleaving samples from adjacent angles within the plane, each sinogram has 192 samples per angle, and a total of 168 projection angles. This results in an in-plane linear sampling distance of 1.2 mm.

The energy window of the detector was set for the entire study to 350−650 keV, and coincidence timing window was set to 6 ns (see Discussion).

Reconstruction Algorithms. Two image reconstruction algorithms were employed.

The first reconstruction algorithm was filtered back-projection of the 2D sinograms rebinned from 3D ones with the aid of Fourier rebinning algorithm (FORE-2DFBP).[15] FORE-2DFBP was performed with a ramp filter cutoff at the Nyquist spatial sampling frequency (0.5 mm^{-1}).

The second algorithm was ordered-subset expectation maximization followed by maximum a posteriori estimation and applied to 3D sinograms (OSEM3D/MAP).[16,17] OSEM3D/MAP reconstruction protocol included two OSEM3D (14 subsets in each) and eighteen MAP iterations optimized for uniform resolution.

Radionuclide and Protein Labeling. ^{124}I was purchased from IBA Molecular, VA. The radionuclide was supplied in the form of sodium ^{124}I solution in 0.02 M NaOH, 0.3−2.7 μL/MBq. Nominal radiochemical purity: 95% (<5% of iodate and diiodate by HPLC). Nominal radionuclidic purity: >99% at calibration (<0.5% of ^{123}I; ^{125}I: none detected, by HPGe gamma spectroscopy). Chemical purity: Te < 1 μg/mL by UV−vis spectroscopy.

Model human recombinant proteins (enzyme replacement therapy candidates) were expressed at Shire HGT (Cambridge, MA). The proteins were labeled with ^{124}I, up to 185 MBq/mg, as described below.

Direct radioiodination was carried out using Iodo-gen precoated iodination test tubes (Pierce 28601) at pH = 7.4, 25 °C for 5−40 min, depending on the protein, with subsequent metabisulfite treatment, desalting and purification of the iodinated protein by size exclusion HPLC (SEHPLC).

Loading per iodination tube: 0.25 M Na phosphate buffer solution, 0.05 mL; protein (6−50 mg/mL), 0.05 mL; [^{124}I]NaI, from 2.74 to 9.58 MBq (in 0.02−0.07 mL). After the iodination, the reaction mixture was transferred to a polypropylene tube containing 1.0 ± 0.2 mg of dry sodium metabisulfite to deactivate the oxidants present in the aqueous phase. The solution was then centrifuged at 5 krpm for 1 min, and the iodinated protein was isolated by SEHPLC using BioRad Bio-Sil SEC 125 column, 80 × 7.8 mm, with UV (wavelength 280 nm) and gamma radioactivity detection. Elution buffer: 20 mM sodium citrate, pH = 6.5, in 0.9% NaCl.

Alternatively, the reaction mixture was desalted by size exclusion chromatography on Sephadex G-25 and analyzed by SEHPLC.

The eluted fractions were analyzed by SEHPLC using a 300 × 7.8 mm Bio-Sil SEC 125−5 column. The amount of protein in the fractions was determined on the basis of the UV absorption at 280 nm. Yield by protein: 60−100%, depending on the protein. Radiochemical yield (by ^{124}I): intact fraction, 30−95%, depending on the protein. Radiochemical purity: >99% by total protein. Where necessary, the solutions of radioiodinated proteins were concentrated on a 3 kDa membrane (Centricon, Millipore, MA).

The radiolabeled preparation was mixed with a calculated amount of unlabeled protein to obtain, for each animal, an injection dose containing 1.00 ± 0.05 mg/kg of protein and 1.85−41.5 MBq of ^{124}I. The solution was distributed into 0.5 mL injection syringes. The total administered volume was 0.05−0.15 mL (rat) and 0.1−0.15 mL (monkey), depending on the injection route.

Phantom Imaging. To investigate the image resolution and count-rate performance of the imager with respect to ^{124}I, phantoms of two types were used, along the lines of the National Electrical Manufactures Association (NEMA) NU 2-2001 and NU 4-2008 standards of performance evaluation for positron emission scanners.

A thin capillary phantom ("line source") was constructed using a high precision glass capillary with a 0.19 mm internal diameter and a 36 mm length. The capillary was filled with an aqueous solution containing 2.5 MBq of ^{124}I. Then, the ends of the capillary were sealed with Parafilm and paraffin, and the capillary was positioned inside a glass tube (13.74 mm internal diameter and 1.016 mm wall thickness) filled with water. Phantoms of the same type were used to measure the spatial resolution of the imager with 1.4 MBq of ^{18}F and 4.2 MBq of ^{64}Cu.

A "volume" phantom, a 5.1 cm diameter ×12.7 cm tall acrylic cylinder with a wall thickness of 3.5 mm, was filled with 198 mL of water containing 83.62 MBq of ^{124}I.

Image Spatial Resolution and Noise Measurements. The line source was placed near the center of the camera bore within 1 cm from the axis (avoiding the exact center of the scanner where the sampling density of the LORs may be very high) and in the periphery (5 cm radial offset), and aligned either along the axial direction or orthogonally in a tangential orientation. The source was imaged in each position for 20 min.

The acquired data were reconstructed into 128 × 128 × 63 image voxel matrix using FORE-2DFBP and OSEM3D/MAP, the latter with a smoothing parameter β value of 0.447, which corresponds to 1.8 mm full width at half-maximum (FWHM) of the Gaussian smoothing function applied to the neighboring voxels. The in-plane pixel size was set to be 0.38 × 0.38 mm. The axial thickness of the plane is fixed at 1.2 mm.

To determine the radial, tangential and axial spatial resolutions, the profile of the line-spread function (LSF) along the corresponding direction was drawn across the image of the line source. The width of each profile at right angle to the direction of the measurement was approximately 6 mm in order to reduce the measurement variability. The FWHM of both Gaussian-fitted and unfitted LSF were used as the measures of spatial resolution.

Due to the biexponential shape of the positron range distribution,[11,18] some distortion of the Gaussian shape of the LSF can be expected. Therefore, to fully and quantitatively characterize the LSF and spatial resolution over all spatial frequencies, the modulation transfer function (MTF) was employed. The MTF was calculated by taking the 2D Fourier transformation of the LSF and by normalizing the amplitude. There is a basic connection between MTF and FWHM that can be demonstrated[19] using a bar pattern having a width of 0.6 times FWHM of the LSF, in which (a) the pattern is no longer resolvable, and (b) the MTF amplitude for the corresponding spatial frequency drops below 0.1.

The volume phantom filled with 33.3 MBq of ^{124}I was used to compare the noise levels obtained with each reconstruction protocol. The noise level in the reconstructed image was estimated as a ratio of the standard deviation to the average concentration of the activity (kBq/mL) in the region of interest (ROI) of 500 pixels. The values were measured and averaged over ROIs drawn in ten slices of the volume phantom.

System Sensitivity. The effective sensitivity of the system was measured in the center of the field of view with a cylindrical volume phantom placed along the axis of the camera. The cylinder was uniformly filled with an aqueous solution of 11.3 MBq of ^{124}I. This activity was sufficiently low to consider dead-time count losses negligible (see Results). The duration of the image scan was 10 min. The value of the system sensitivity with ^{124}I was calculated by dividing the true coincidence counts per second by the activity in the field of view as measured by a calibrated external gamma counter. The true event count-rate was obtained by subtraction of random and scatter events from prompt coincidences. Scatter coincidences were calculated using the measured scatter fraction (see below). Signal attenuation in the water filling the phantom and the material of the phantom walls was also taken into account as

$$R_0 = R \cdot \exp[2 \sum_i \mu_i x_i] \quad (1)$$

where R and R_0 are true count rates in the presence and in the absence of attenuation, respectively, and μ_i is an attenuation coefficient of the medium having thickness x_i.

Count-Rate Performance. A cylindrical volume phantom (the dimensions of which closely resemble the body of a laboratory rat) was used to measure true, random and scatter coincidences, as well as single event rates at different activities of ^{124}I ranging from 0.37 to 83.62 MBq. The range was covered by multiple measurements in the course of ^{124}I decay from 83.62 to 0.37 MBq over 19 days.

The phantom was placed along the axis of the camera in the center of the field of view extending 2.4 cm beyond the field of view at both sides. Thus, the data incorporates the effects of the out-of-field activity from the parts of the phantom located outside of the imaging area (as in a typical animal experiment). Phantom images were acquired over 10 min each.

The random coincidences were subtracted from the prompt events giving histogrammed total coincidence events (true + scatter events). The latter were then corrected for detector dead-time and normalized for detector efficiency and crystal interference pattern.

In order to evaluate the effect of subtracting the random and scatter count components from the total number of coincidences on the noise values, the noise-equivalent counting rate (NEC) was calculated based on the following equation:

$$\mathrm{NEC} = \frac{R_t}{1 + \frac{R_s}{R_t} + 2k\frac{R_r}{R_t}} \quad (2)$$

where R_t, R_r and R_s are true, random and scatter count-rates, respectively; k is a fraction of the projection subtended by the cylinder and is equal to 0.23. NEC is considered to be an image quality factor since it directly proportional to the signal-to-noise ratio (SNR).[20] Therefore, it can be seen that NEC equals the reduced R_t that without random and scatter components would produce the same SNR as the given R_t does. The scatter counting rate was derived using the scatter fraction (SF) definition as the ratio of the amount of scatter to total events (true + scatter coincidences). The SF, in turn, was calculated at a sufficiently low counting rate (11.1 kBq/mL), at which random coincidences, dead-time effects, and pulse pile-up are negligible. To this end, the sinogram profile was used to estimate the amount of (a) scatter events within the field of view and (b) total events within the volume phantom. Coincidences outside the phantom were considered to arise from scattering, after the subtractions of random events. The scattered radiation within the object was

assumed to follow the Gaussian distribution[2] obtained by fitting sinogram profiles outside the phantom. SF was measured for each slice and then averaged. The number of true events was then calculated by subtracting the scatter from total coincidences.

Corrections. All acquired data were corrected for radioisotope decay, detector dead-time, random and scatter coincidences, attenuation, and also normalized for geometric differences of the locations of detector crystals and their individual efficiencies.

Dead-time and random coincidence corrections were based on the current measured single event count-rate.

To apply the correction for attenuation, a transmission scan was obtained for each emission image without changing the phantom (or animal body) position. A point source containing 185 Mbq of ^{57}Co (Eckert & Ziegler Isotope Products, Valencia, CA) was installed in a transmission source holder rotating around the animal port in a helical trajectory. Typically, each transmission scan was acquired over 10 min. The transmission list-mode data were rebinned using a single slice-rebinning (SSRB) algorithm, followed by attenuation calibration and segmentation.

The emission scatter correction was carried out by direct calculation of the scatter distribution, taking into account the source and object geometries.[21,22]

Data normalization for the geometry and counting efficiency of the individual crystals was carried out using a component based method described by Casey et al.,[23] using a rotating ^{68}Ge point source.

Animal Studies. Normal 150−250 g Sprague−Dawley rats and 2.8−5.6 kg cynomolgus monkeys (Macaca Fasicularis) were used to investigate protein biokinetics after subcutaneous (SC), intravenous (IV) and intrathecal (IT) administrations. Model proteins were injected at doses and ^{124}I activities described in Radionuclide and Protein Labeling. All animal experiments were carried out in accordance with institutionally approved protocols.

Rats. IV administration: Animals were set in a restrainer. A heparinized 3 in. catheter (BD 387334) was inserted into the tail vein and connected with a T connector (Abbott 1157218). Sodium pentobarbital, 35 mg/kg, was injected through the T connector cap and flushed with 0.5 mL saline. Then, animals were set on a MicroPET bed and injected with ^{124}I-labeled model protein through the T connector cap (flushed with 0.5 mL of saline) simultaneously with the start of dynamic imaging procedure.

SC administration: Animals were anesthetized with sodium pentobarbital (50 mg/kg, IP injection), placed on the MicroPET bed, and injected with ^{124}I-labeled model protein (front extremity, under a distal dorsal skin fold) with the start of dynamic imaging occurring simultaneously. In the groups receiving multiple injections, the first SC administration was into the right extremity, the second administration was into the left, and the third administration was into the right.

Monkeys. Over the entire duration of the study, the animals were segregated from other NHPs and housed in a separate room at the MGH primate facility.

At the housing site, the animals were sedated with ketamine/xylazine IM and then transported to the imaging site, where the animals were temporarily housed in standard NHP cages.

At the imaging site, each animal was first sedated with ketamine IM (if and as needed), positioned on a custom polycarbonate imaging bed, and given continuous Isoflurane/O_2 anesthesia. Heart rate, breathing rate and CO_2 content in the exhaled air were monitored continuously; isoflurane flow was adjusted as needed. Animals were given nonradioactive iodine (0.2 mL, 15 mM NaI) as a SC injection immediately before the study to suppress ^{124}I uptake in the thyroid. The radioiodinated proteins were administered intravenously (IV), subcutaneously (SC) or intrathecally (IT).

IV administration: A catheter equipped with a T connector was installed in the saphenous vein. The animals were set on a MicroPET bed and positioned for dynamic imaging of the lower thoracic (heart and liver) area. A transmission image was acquired before the injection. Then, the protein solution was administered through the T connector cap and flushed with 1 mL saline simultaneously with the start of the dynamic imaging procedure.

SC administration: The animals were set on a MicroPET bed and positioned for dynamic imaging of the injection site (shoulder) area. A transmission image was acquired before the injection. Then, the ^{124}I-labeled model protein was administered subcutaneously in the external shoulder area. The dynamic imaging procedure was started immediately.

IT administration: The animals were sedated; the injection point was shaved, wiped with 70% alcohol, and treated with Betadine. Injections were carried out in a prone position with a support providing a vertically bent, exposed injection area (atlanto-occipital joint for ICM, L4-L5 area for IL). A 27G 1 in. needle equipped with a 3 in. transparent catheter with a T-cap was inserted between the vertebra until CSF flow is detected in the catheter. A small volume (0.1−0.2 mL) of CSF was drawn through the catheter. Then, the ^{124}I-labeled model protein solution was injected through the T-cap, and the latter was flushed with 0.05 mL of the previously drawn CSF. The needle was withdrawn and the injection site was immediately imaged.

The animals were set on a MicroPET bed in a supine position, and the bed was positioned for dynamic imaging of the injection site area. The dynamic imaging procedure was started immediately and continued for 20 min followed by 5 min (rats) or 10 min (monkeys) per body section static scans performed in 1, 2, 4, 8, 24, 48, 96, and 192 h.

The data were reconstructed into the image matrix with the pixel size of 0.95 mm and fixed slice thickness of 1.2 mm using OSEM3D/MAP, with the hyperparameter β values of 0.085 and 1.516 for rats and monkeys, respectively. The data were also reconstructed with FORE-2DFBP to ensure that the numerical data derived from OSEM3D/MAP and FORE-2DFBP reconstructed images were identical.

Whole body images were composed of section images that were acquired with 12 mm overlapping.

To measure the total ^{124}I activity (kBq) in a tissue, the whole organ was taken as a ROI. The activity concentration (kBq/mL) was determined by averaging over multiple ROIs drawn within the tissue of interest. The data obtained for each protein will be published in detail elsewhere.

Workstations and Software. Data acquisition, prereconstruction and reconstruction were carried out on a Dell Precision PWS690 workstation (3 GB RAM and 8 Xeon 3.20 GHz processors running under 64 bit Windows XP (Microsoft, WA), using Siemens microPET Firmware/Software, release 2.4.

All subsequent image processing and analysis were performed on nonhost workstations using the ASIProVM software (Siemens/CTI Concorde Microsystems, TN) under Windows XP (Microsoft, WA) and MacOS 10.5 (Apple, CA) and Amide[24] running under MacOS 10.5 (Apple, CA).

Table 1. Spatial Resolution (FWHM) in the Center and the Periphery of the Field of View[a]

	center of the FOV[b]			5 cm radial offset[c]		
method of reconstruction and measurement	radial	tangential	axial	radial	tangential	axial
FORE-2DFBP						
Gaussian fitted	3.24 ± 0.08	3.37 ± 0.14	3.69 ± 0.15	3.93 ± 0.21	3.67 ± 0.23	4.59 ± 0.25
effective (no fitting)	2.90 ± 0.03	3.14 ± 0.06	3.43 ± 0.09	3.83 ± 0.22	3.50 ± 0.12	4.22 ± 0.08
MTF-estimated	3.00 ± 0.06	3.13 ± 0.07	3.40 ± 0.08	3.87 ± 0.37	3.49 ± 0.15	4.32 ± 0.09
OSEM3D/MAP						
Gaussian fitted	2.52 ± 0.04	2.51 ± 0.06	3.10 ± 0.05	2.66 ± 0.07	2.59 ± 0.06	3.15 ± 0.09
effective (no fitting)	2.41 ± 0.01	2.39 ± 0.03	2.92 ± 0.04	2.60 ± 0.08	2.50 ± 0.05	2.96 ± 0.15
MTF-estimated	2.51 ± 0.02	2.46 ± 0.04	2.70 ± 0.04	2.64 ± 0.07	2.53 ± 0.03	2.74 ± 0.06

[a] Values are given in mm. Errors are expressed as SD. [b] In the center of the field of view (FOV; within 1 cm off the axis), the data were averaged over three axial positions. [c] For a radial offset, the data were additionally averaged over two radial positions of the line source.

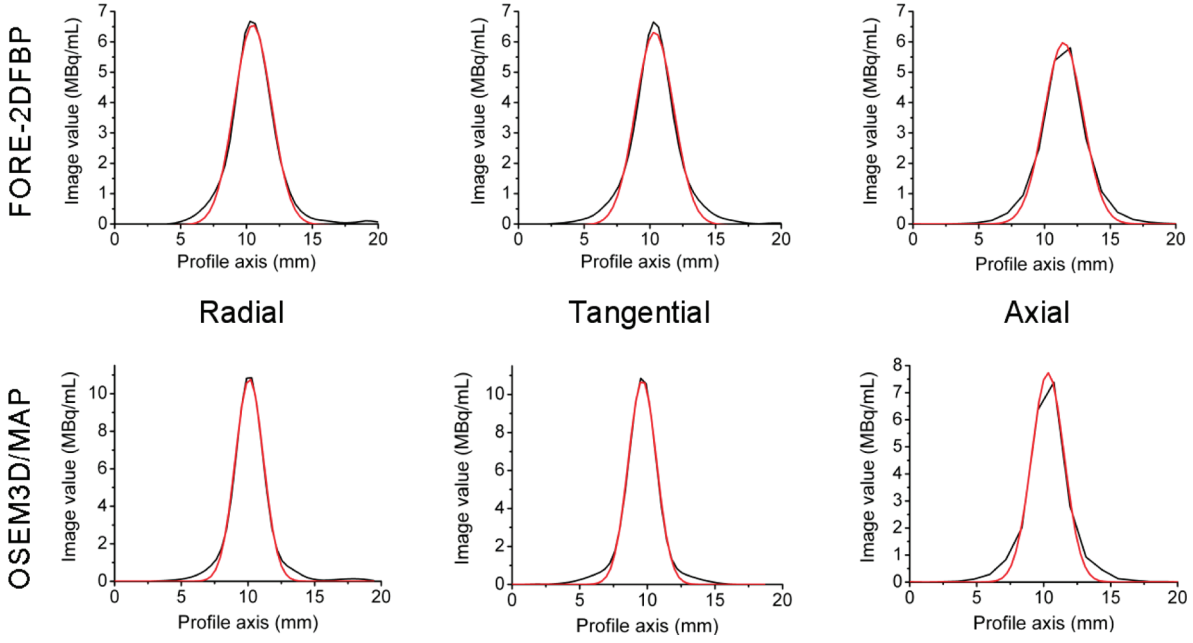

Figure 1. Line spread functions. Profiles were taken in three directions across FORE-2DFBP and OSEM3D/MAP images of the line source placed in the center of the field of view. Gaussian fitting is depicted in red.

RESULTS

Spatial Resolution. Spatial resolution is a composite characteristic of the image quality. The value of spatial resolution depends on the physical features of the imager as well as on the decay characteristics of the radionuclide and the reconstruction procedure. To address the latter factor, both analytic FORE-2DFPB, and iterative OSEM3D/MAP reconstruction algorithms were used in this study to examine the algorithm impact. The transaxial (radial and tangential) and axial resolutions were measured as FWHM. The results are summarized in Table 1.

Figure 1 depicts the LSFs as profiles taken in three directions across FORE-2DFBP and OSEM3D/MAP images of the line source placed in the center of field of view.

The tails of the LSFs indicate the partially non-Gaussian nature of these distributions, most likely due to the exponential shape of the positron range blurring.[18] Because of this non-Gaussian nature, characterizing the LSF with single numbers, such as FWHM or the root-mean-square deviation, does not provide a complete description of the actual resolution.

Unlike FWHM, which characterizes only the limiting resolution (i.e., the minimum resolvable distance between two objects), MTF distribution characterizes the spatial resolution of the imaging system with respect to both coarse (low frequencies) and fine (high frequencies) details.[19] MTFs for the transaxial and axial directions calculated for the FORE-2DFBP and OSEM3D/MAP reconstructions of the line source are shown in Figure 2.

The data presented in Table 1 and Figure 2 suggest that OSEM-3D/MAP reconstruction enables better resolution than FORE-2DFBP, not only for high frequencies (which correspond to fine image details) but also for the entire frequency range. Although the graphic noise patterns in the OSEM3D/MAP (granular) and FORE-2DFBP images were entirely different (granular and starlike, respectively), the formally calculated noise levels for both algorithms were essentially the same: 30.2% and 34.5% respectively.

Both reconstruction algorithms showed a somewhat higher value of in-plane resolution as compared to the axial resolution. It

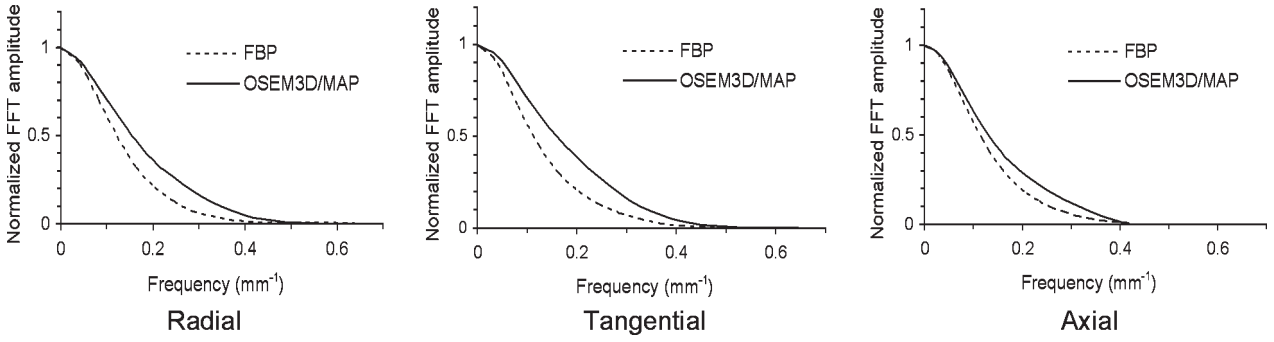

Figure 2. MTF for two reconstruction algorithms, FORE-2DFBP and OSEM3D/MAP, in transaxial and axial directions.

Table 2. In-Plane Resolutions (FWHM) in the Center of the Field of View, Positron Ranges and Half-Lives for Three Positron Emitters[a]

isotope	half-life, h	mean range in water, mm (β^+_{max} energy, MeV)[34]	FWHM, mm
iodine-124	100.2	2.3 (1.53)	3.31 ± 0.16
		3.5 (2.14)	
fluorine-18	1.8	0.6 (0.63)	2.37 ± 0.04
copper-64	12.7	0.6 (0.65)	2.44 ± 0.04

[a] Errors are expressed as standard deviations.

was reported that some degradation of the axial resolution in FORE-2DFBP might be caused by the axial parallax or depth-of-interaction (DOI) effect due to crystal penetration of oblique LORs in the axial direction.[25] The effect is most significant in cameras with large aspect ratio or large acceptance angles.[26] The significance of this effect in microPET P4, where the acceptance angle is relatively small (16.8° to the transaxial plane) and the crystal depth of interaction is 4.58 cm, is negligible for geometrical reasons.

Some image degradation may be caused by imperfections of the conventional Fourier rebinning in 2-dimensional reconstruction techniques.[15] However, this may only be applicable to FORE-2DFBP, whereas our data show deterioration of the axial resolution in both FORE-2DFBP and OSEM3D/MAP. Therefore, the lower axial resolution observed in our study is more likely related to the fixed image slice thickness (1.2 mm) of the imager that may result in an insufficient sampling in the axial profile.

Some degradation of the reconstructed image resolution in the periphery of the imaging space (5 cm radial offset) was observed for FORE-2DFBP in both transaxial (21.3% radial and 8.9% tangential) and axial (24.4%) directions. This may be attributed to the geometry of the scanner that suggests increased DOI effects at high radial offsets and changes in the coincidence response function in a close proximity to one of the detectors. The former effect results from the angulation between the detector crystals and the lack of knowledge about the depth at which the photon-crystal interaction has occurred.[19] Unlike FORE-2DFBP, OSEM3D/MAP showed an almost uniform resolution across the field of view of the scanner, which may be attributed to the use of the **P**-matrices and blur kernels in each iteration step, which takes into account the geometry of the camera and DOI effects in both the transaxial and the axial directions.

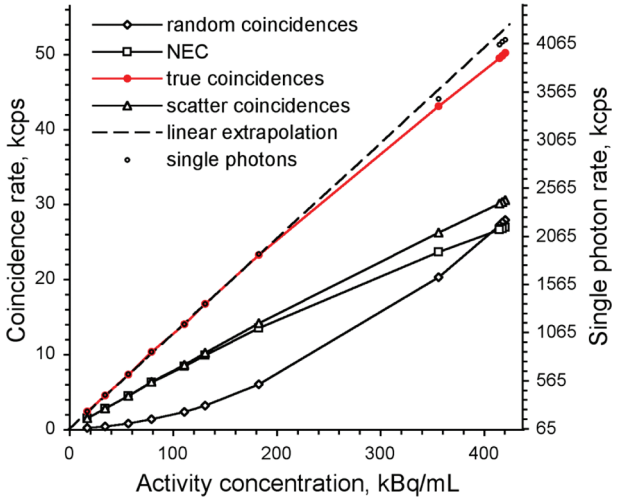

Figure 3. Count-rate performance for ^{124}I on the microPET P4 scanner. Relative errors for true coincidences and single photon count-rate are 0.36% and 0.05%, respectively.

For small animal imaging devices employing small discrete detector elements, the effect of high-energy positron ranges on the resultant system resolution becomes substantial.[18] This can be readily seen in Table 2, where spatial resolutions measured for ^{124}I and two other conventional positron emitters (^{18}F and ^{64}Cu) are shown. Although the positron range of ^{124}I significantly differs from those of ^{18}F and ^{64}Cu, the effective spatial resolutions of images taken with ^{124}I and these radionuclides were similar and sufficiently low to resolve all large organs in mice, and practically all organs and structures in rats and larger animals.

Count-Rate Performance. A well-defined signal dependence on the label activity is mandatory for quantitative imaging studies.

In the absence of any imager and radionuclide-related factors affecting the counting efficiency, the dependence is expected to be linear. In our studies, a near-perfect linearity of the "true" coincidence count-rate was observed at the ^{124}I concentration of up to 225 kBq/mL and at the total activity in the field of view and adjacent region of up to 45 MBq (Figure 3). The effective imager sensitivity for ^{124}I in the linear range was found to be 1.7 cps/kBq.

As expected, the signal deviates from linearity at higher count rates. Such count loss is most likely a result of two effects that become significant as the count-rate rises: the detection dead-time and multiple coincidences.

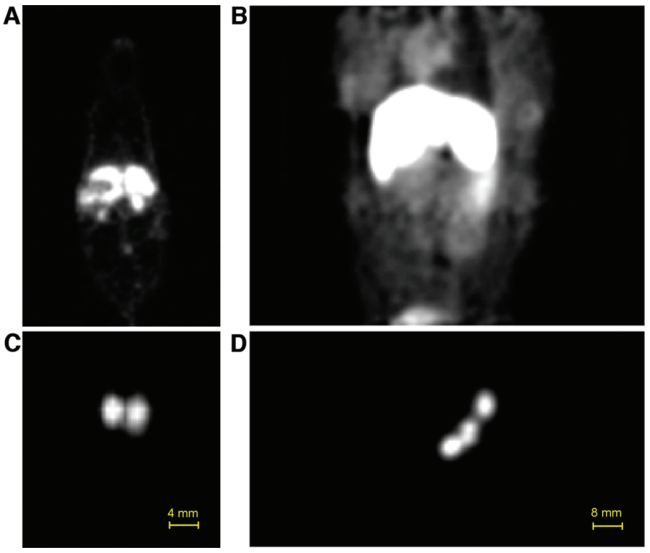

Figure 4. (A) Coronal whole body image of the rat 8 h after IV injection of 12.95 MBq of [^{124}I]α-galactosidase. (B) Coronal image of the monkey's abdomen 4 h after IV injection of 39.96 MBq of [^{124}I]α-galactosidase. (C) Coronal image of thyroid lobes in a rat 48 h after IV injection 18.5 MBq of [^{124}I]α-galactosidase. (D) Coronal image of a group of axillary lymph nodes in monkey 8 h after SC injection of 39.6 MBq of [^{124}I]α-galactosidase.

The detection dead-time (about 320 ns for microPET) and pulse pile-up as one of its manifestations occur due to the finite time required to process the individual detected events. Multiple, more specifically triple, coincidences cannot be unequivocally interpreted and, therefore, are ignored by the imager.

To determine the contribution of each of the above effects, the single photon count-rate was determined (Figure 3). The latter can only be affected by the pulse pile-up. Since the loss of single photon counts was observed in spite of the dead-time correction, both dead-time and multiple coincidences may contribute to the loss of sensitivity at high activity levels. This loss (once measured) can be readily accounted for in animal studies. More importantly, at doses below 45 MBq per animal (in and in the vicinity of the field of view) the data can be used without corrections for nonlinearity.

The overall effect of the high content of single photons present in the emission spectrum of ^{124}I on the true counts can be described with the NEC curve (Figure 3). NEC is the image quality factor that provides a direct link between the image SNR on one hand and the scatter, random and true coincidences count-rates on the other. This correlation is based on the noise effects of subtracting the random and scatter counts from prompt events.[20] Thus, the closer NEC is to the true events counts the better. As compared to a "pure" positron emitter (^{11}C, measured under the same conditions), the deterioration of NEC for ^{124}I is significant.[2] This is a result of the lower abundance of the true events and increased random and scatter counts due to the presence of 602 keV single photons. The activity surrounding field of view (38% for our phantom) also contributes to the scatter background and thereby reduces NEC. However, its effect does not exceed 5% in the roughest approximation according to our calculations (not shown). The total scatter fraction in our experiment was found to be 37.8%.

Model Animal Studies. The performance characteristics of ^{124}I observed in the phantom studies were confirmed in the animal studies, including quantitative investigation of the pharmacokinetics of five model proteins (the pharmacokinetics data will be reported in detail elsewhere). Some examples illustrating the image and data character with ^{124}I-labeled α-galactosidase (candidate for enzyme replacement therapy) are given below.

Figure 4 demonstrates the visual quality and resolution characteristics of the typical images. The distribution of the labeled protein in the rat's body post IV administration is shown in Figure 4A. A well-resolved structure of the liver with two adjacent kidneys can be clearly seen in the slice. Figure 4B illustrates the distribution of the labeled protein molecule in the monkey's abdomen following IV administration. The highest uptake is in the liver, with measurable activity present in the heart and both kidneys. An edge of the bladder can be seen on the bottom of the image. As an illustration of the image resolution with ^{124}I, two lobes of a rat thyroid (anatomical distance 2 mm) are shown in Figure 4C. A group of axillary lymph nodes in the monkey is resolved in Figure 4D.

The typical pharmacological study includes evaluation of the initial transfer of the administered substance from the administration point to the target tissue and other tissues, and, for large molecules and drug delivery systems, of the secondary processes (drug release, macromolecule degradation, etc.). These processes can be fast (e.g., the half-life of some polications in the rodent blood is <1 min) as well as slow (e.g., extravasation of long-circulating macromolecules can continue for several days). Ideally, the imaging label should allow for a detailed investigation of the initial transfer and at least an estimation of the parameters of the (usually slower) redistribution and metabolization rates.

The initial pharmacokinetics of large molecules and nanoparticles is frequently strictly monoexponential.[27,28] Figure 5 illustrates how the kinetics of the fast initial protein clearance from the blood can be determined by PET with ^{124}I from the dynamic imaging data. In this case, the first order process of blood clearance was evaluated by moving frame linearization (Guggenheim method[29]).

In this example, 9.25 MBq of ^{124}I-labeled α-galactosidase was administered IV into a rat. Immediately after the injection, a 20 min dynamic data acquisition was started. The dynamic data array was then split into 1 to 3 min frames. In each frame, ROIs were selected in the vena cava region (red cursor cross in Figure 5A marks the position of ROI). The average activity (kBq/mL) in the ROIs was then determined for each frame (Figure 5A). Excellent data correlation with monoexponential blood clearance was observed over the first 8 min for three different Guggenheim frame lengths (Figure 5B). Regardless of the frame length, the blood half-life was found to be 92 s (parallel lines with equal slopes in Figure 5B). Fitting of the experimental data into theoretical monoexponential curve (regression coefficient $R > 98\%$) is shown in Figure 5C.

The long physical half-life of ^{124}I enables the investigation of fast processes to be combined with evaluation of slower processes in the same study and in the same animal.

Evaluation of a slow process by PET with ^{124}I can be illustrated by the study of protein uptake from the SC injection site (Figure 6). In this example, 40.7 MBq of ^{124}I-labeled α-galactosidase was injected SC in the forearm of the monkey. The entire SC injection site was taken as the ROI. The animal was imaged at multiple time points over 8 days, images were reconstructed as described above, and the total ROI characteristic activities for

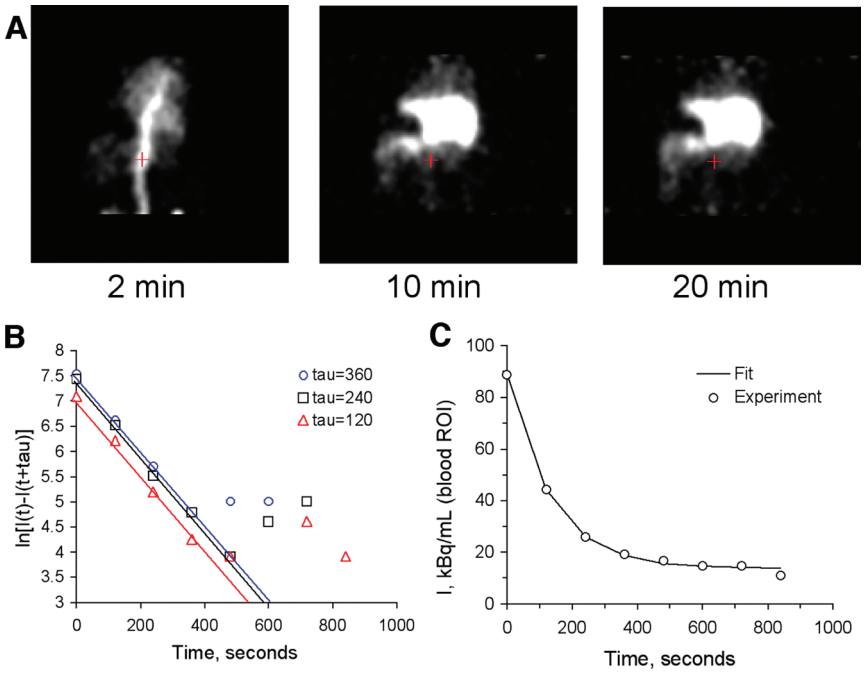

Figure 5. (A) Dynamic coronal images of the abdominal aorta in a rat after IV injection of 9.25 MBq of [^{124}I]α-galactosidase. One minute per frame. (B) Example of moving frame linearization, three different frame lengths. (C) Example of data fitting, $R > 98\%$. $T_{1/2} = 92 \pm 4$ s.

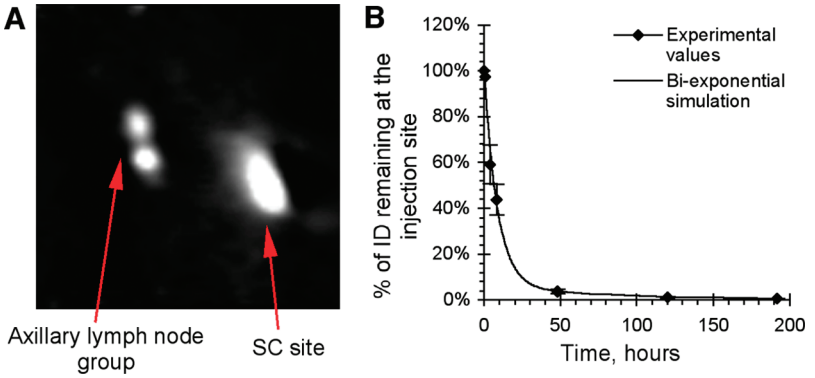

Figure 6. (A) Accumulation of 40.7 MBq of [^{124}I]α-galactosidase in the lymph nodes adjacent to SC injection site. Coronal image of the monkey's forearm 8 h after SC injection. (B) Biexponential fitting of the experimental data on the uptake from SC injection site (ID: injected dose).

each time point was calculated. The data showed that the protein was transferred from the SC injection site to the systemic circulation, at least partially through the adjacent axillary lymph node group (Figure 6A). The uptake was found to be biexponential, with a half-life of 6 h for the major fraction (94% of the injected dose) and 80 h for the residual fraction (Figure 6B). More than 90% of the SC injected doze reached systemic circulation, while a minor fraction of up to 9% was deposited in the adjacent lymph nodes. Interestingly, administration of the same protein in rats (not shown) showed the same character and rate of protein uptake from the SC site.

One of the advantages of ^{124}I as compared to other radionuclides with similar physical half-lives (e.g., ^{111}In) is that intracellular metabolization of radiolabeled biomolecules is not followed by significant retention of the radioactive metabolites in the cell. Thus, iodine clearance from the tissues where the biomolecules had been deposited provides an upper estimate of the biomolecule integrity in the tissues. For an example, Figure 7 demonstrates [^{124}I]α-galactosidase accumulation and metabolization in major organs of the rat over 10 days following three consecutive IV (Figure 7A) and SC (Figure 7B) injections.

Thus, PET imaging with ^{124}I enables acquisition of essentially the same data as conventional tissue sampling studies in a nonterminal experiment that requires a significantly smaller number of animals that can be (if necessary) used repeatedly.

DISCUSSION

The availability of high-resolution PET imagers and the recent emergence of commercial suppliers of positron emitting isotopes make PET a feasible and advantageous alternative to the conventional (tissue sampling) pharmacokinetics studies.

Iodine-124, in view of the long physical half-life and the known behavior of iodine in vivo, is of great interest as a label for long-term (days) pharmacokinetics studies that are needed in the

dx.doi.org/10.1021/mp100358f |*Mol. Pharmaceutics* 2011, 8, 736–747

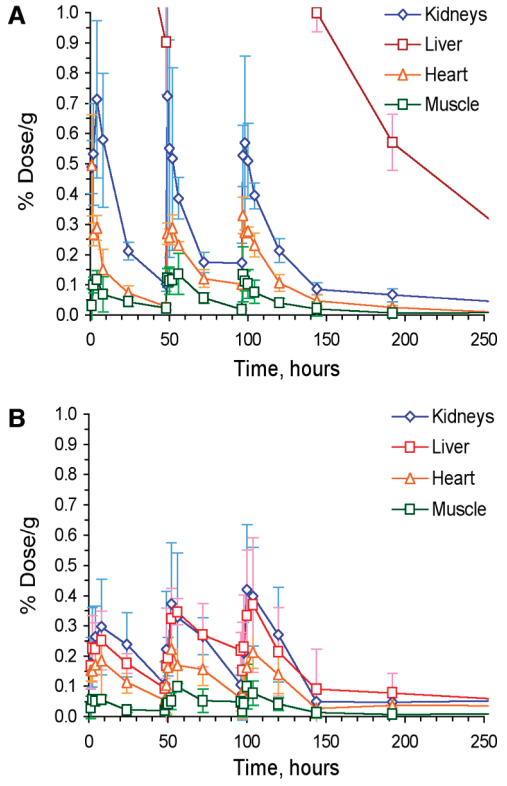

Figure 7. α-Galactosidase deposition and metabolization in the heart, liver, kidney and muscle of the rat over 10 days following three serial IV (A) and SC (B) injections.

development of novel therapies based on large biomolecules, nanoparticles and other drug delivery systems.

Our data show that, in spite of some properties of ^{124}I that may be of concern in other applications of this radionuclide, in pharmacological imaging of the pharmacokinetics of large molecules and drug delivery systems they are clearly outweighed by the benefits provided by this isotope.

One of the features of ^{124}I is (i) the high energy positron emission accompanied by (ii) significant coemission of single photons in the same energy range with annihilation photons, partially in the same decay events ("third photons"), which may affect image resolution and, more generally, the quality of the imaging data.

The comparison of spatial resolutions obtained for ^{124}I and two other positron emitters, ^{18}F and ^{64}Cu (Table 2), suggests that the higher energy and the respectively longer range of ^{124}I positrons do affect the resolution but not as dramatically as to result in a significant limitations in the radionuclide use. Within the context of pharmacological imaging, the FWHM value of 3.31 mm (^{124}I) does not introduce any significant limitations in the method feasibility as compared to the 2.37 and 2.44 mm for ^{18}F and ^{64}Cu, respectively. All three radionuclides are equally feasible for quantitative imaging of major organs in mice and practically all organs in rats and other animals (except, perhaps, for imaging of groups of lymph nodes located at submillimeter distances from each other, which is rarely necessary). We should note that the spatial resolution measurements were carried out in water, which differs in density from live tissues. Positron diffusion impact on the spatial resolution is inversely proportional to the density of the absorber. Therefore, lower values (better resolution) can be expected in vivo in dense tissues, e.g., bone, and higher ones in the lungs.

Because of the complex decay of ^{124}I that produces several single photons, the effective sensitivity of the imager to true events for ^{124}I should be lower than for "pure" positron emitters. Almost 50% of all positron-producing decays of ^{124}I contain an extra single photon (602 keV) in the same cascade. The emission of this photon along with two annihilation photons reportedly occurs within a time interval that is shorter than the discrimination window of PET scanners (the exact time interval has not been published). This photon may be the major cause of triple coincidences resulting, depending on the camera geometry, in the loss of sensitivity (19% for microPET P4 according to our estimations) even at relatively low activities.[10] If one of the annihilation photons is absorbed, a coincidence between the second one and the 602 keV photon from the same decay can occur. This spurious coincidence is indistinguishable from a standard scattered event and is a subject of scatter correction.[11] This is another cause of a somewhat higher amount of the scatter fraction with ^{124}I, 37.8% as compared with 25.5% measured[2] for ^{11}C, a pure positron emitter.

The high content (60.5%) of 602 keV single photons in the emission spectrum may also result in their coincidences with (i) another single photon and (ii) one of the annihilation photons from a different decay.[10,13] These coincidences may be corrected by means of randoms subtraction, for which it is irrelevant whether the detected events related to annihilation photons had originated from different positrons or single gamma emissions. The random coincidence correction based on singles rates (which is implemented, e.g., in microPET P4) will be just as accurate with ^{124}I as with other radionuclides.[13] Some methods of background correction can also be applicable.[14]

Notably, in theory the upper energy threshold and timing window of the scanner can both be optimized to minimize the effect of 602 keV photons. The efficiency of such discriminations is defined by the energy and timing resolutions of the detectors, NEC being the criterion of merit. In this respect, the average energy resolution of 26% across all crystals in the microPET P4 system[2] is insufficient for significant energy-based discrimination, thus energy discrimination was not utilized. The coincidence timing resolution of the microPET P4 scanner is 3.2 ns,[2] but the scanner supports only 2, 6, 10, and 14 ns time windows. Although it would be desirable to minimize the window to exclude as many multiple coincidences as possible, settings below 6 ns significantly reduce the sensitivity and still do not enable the discrimination of the single photons generated in the same decay cascade as the positron. Therefore, the timing window in this study was set at 6 ns.

The random coincidences become more noticeable at high activities because their rates are proportional to the respective single photon count-rates. In addition, as mentioned above, the high count-rates of the true coincidences and 602 keV single photons contribute to the increased counts of triple coincidences between them. Such triple events lead to the rejection of valid events by the imager. These and the dead-time losses should and do result in the extra loss of sensitivity at high amounts of ^{124}I in the camera's field of view (Figure 3). If not corrected for, such deviations from signal linearity will impair the quantitative analysis at ^{124}I concentrations higher than 225 kBq/mL. This value, however, is specific for microPET P4 scanner (and for the phantom used) and may be higher or lower for other imagers. Notably, multiple coincidences and pulse pile-up effects at high activities are not unique to ^{124}I. For pure positron emitters, count losses relate to single 511 keV photons, the count-rates of which

are higher and, under certain circumstances, may be significant at even lower activities than for ^{124}I (see, for example, Figure 10 in ref 10).

Overall, the results of our performance study with ^{124}I suggest that most of the detection events related to the single photons accompanying the positron decay are recognized and can be accounted for as ordinary random and scatter coincidences. The correction for them using the means implemented in most PET scanners will restore the normal background and provide the image quality required for quantitative analysis. At high concentrations of ^{124}I, the accuracy of the analysis will be impaired by gradual nonlinear loss of counts, which should be accounted for. Relatively low abundance of true coincidences with ^{124}I will result in lower NEC and SNR than for "pure" positron emitters. The latter, however, can be compensated for with increased acquisition time.

The results of imaging studies with ^{124}I labeled proteins in small (rat) and large (monkeys) animals are in agreement with the results of the phantom study, demonstrating good delineation of protein accumulating organs (e.g., heart, liver, kidneys in Figure 4) and resolution of small structures located within single millimeters from each other, such as thyroid lobes in rats and individual lymph nodes in rats and monkeys (Figure 5). Satisfactory data quality was achieved at the administered doses between 1.85 and 27.38 MBq per animal for rats and ca. 39 MBq per monkey (static image acquisition, 5−10 min duration). Imaging of fast blood clearance using short dynamic time frames (1 min) was feasible at 9.25 MBq per rat or higher. Thus, pharmacological imaging with ^{124}I generally does not require using high activities at which the data need to be corrected for nonlinearities as discussed above. Extrapolating to larger animals, the suitable administered ^{124}I dose is expected to be ca. 3.7−9.25 MBq per kg of body weight. For humans, the dose is more likely to be limited by dosimetry considerations than nonlinearities in data acquisition at high activities.

One of the factors affecting the spatial resolution of the image is imperfection of the reconstruction algorithms. To date, several reconstruction algorithms have been developed, each having intrinsic strengths and weaknesses.

Among others, FORE-2DFBP has advanced in popularity giving reasonably satisfactory images during a relatively short computation time. FORE-2DFBP is recommended by the National Electrical Manufactures Association (NEMA) for comparative evaluation of the spatial resolution of images obtained on different PET scanners.[30] However, the outcome of this algorithm is very sensitive to the projection sampling distance during Furier transform, and is defined by the choice of reconstruction filter and its cutoff frequency. The latter necessitates a trade-off between the spatial resolution and SNR in the image. Also, the angular and linear sampling distances in FORE-2DFBP are restricted by the design features of the imaging system, and, as a result, they do not reach the theoretically achievable values. Aliasing and streaking artifacts commonly encountered with FORE-2DFBP may also significantly distort delineation of organ boundaries and, therefore, hinder the selection of regions of interest for data extraction.

The alternative, 3D iterative reconstruction methods, particularly OSEM3D/MAP available with MicroPET P4, are free from the above drawbacks of FORE-2DFBP. In our study this resulted, in particular, in a better spatial resolution recovery with OSEM3D/MAP at nearly the same noise level as with FORE-2DFBP (Table 1). A more accurate and uniform resolution across the entire field of view provided by OSEM3D/MAP, which is particularly beneficial for studies in larger animals, is a result of incorporation of the imager geometry and parameters of the individual detectors in the reconstruction. Iterative methods are computation-demanding, but with the development of faster hardware the computation time required for OSEM3D/MAP reconstruction is less limiting than in the past. We believe, OSEM3D/MAP is presently a superior alternative to FORE-2DFBP in the pharmacological studies with ^{124}I.

The data of this study and seven pharmacokinetics studies utilizing ^{124}I labeled proteins (four in rats, three in monkeys, details to be published elsewhere) suggest that PET studies of the large molecule pharmacokinetics with ^{124}I not only provide data in the format suitable for pharmacological evaluation and modeling, but also provide several advantages as compared to the conventional studies. Whole body PET imaging provides data on all organs and tissues as opposed to selected tissue samples; thus, all patterns of the test substance behavior (including unexpected ones) are readily revealed on image examination. The same patterns are then quantitatively evaluated based on the same data, without the need for an extra study. Very fast processes (such as blood clearance) that are difficult to investigate by tissue sampling due to the short sampling intervals are readily studied by imaging. With ^{124}I, these processes can be investigated in the same experiment as slow processes, which reduces the overall study length. Since several measurements can be taken over time from the same animal (and the animal can later be reused), the same amount of information can be acquired using a considerably smaller number of animals. The latter is especially significant for experiments utilizing large and rare animals.

Another useful feature of ^{124}I relates to the character of biological processing of radioiodinated compounds, in particular proteins. The labeling reagents induce ortho/para directed iodination of activated aromatic rings (predominantely phenols). The stability and biological faith of the label depends on the character of the iodinated moiety. In proteins, iodinated tyrosine is generally stable in the extracellular environment. Intracellular (lysosomal) fragmentation of the iodinated biomolecules results in the formation of iodinated fragments succeptible to deiodination by various oxido-reductases, including specialized deiodinases,[31] eventually resulting in free intracellular iodide. The latter is rapidly released into the extracellular environment. The appearance of iodide in the systemic circulation is readily detected in the images, as iodide is rapidly cleared from plasma by kidneys and gastric iodide pump. (The latter, unlike the thyroidal and salivary pumps, is not easily inhibited by administration of "cold" iodide usually given to the animals to block iodine accumulation in the thyroid.) The process of iodide clearance from plasma then includes iodide release into the stomach, reuptake in the gut and renal clearance.[32,33] Under most circumstances, the steady-state iodide concentration in the blood plasma is low, and can be measured directly and subtracted from the image data for every tissue based on the known blood content. As a result, long-term imaging data obtained with ^{124}I (as in Figure 7) usually include the following readily discernible periods: (i) initial distribution; (ii) mixed distribution and metabolization, beginning of label clearance; and (iii) metabolization and label clearance. The beginning of the second period is readily detectable by the appearance of radioactivity in the stomach wall, and of the third period, by blood analysis. The pharmacokinetics of the original radioiodinated form can be determined from the data obtained during the first period. The second period provides C_{max} and

T_{max}, while the last period provides initial estimates of the biomolecule stability and metabolization rates in organs and tissues.

The quality of the imaging data of the phantom and model animal studies lead us to the following conclusions.

CONCLUSIONS

Both phantom and model animal studies suggest that ^{124}I is an excellent label for pharmacological PET studies.

The high energy and long range of the ^{124}I positrons do not significantly affect the spatial resolution, and, in the context of pharmacological studies, do not introduce significant limitations to the suitability of ^{124}I as compared to other positron emitters.

Both OSEM3D/MAP and FORE-2DFBP reconstruction protocols can be useful for image reconstruction. OSEM3D/MAP is more computation-intensive than FORE-2DFBP, but gives better resolution at the same noise level.

The optimal dose of ^{124}I for small animals is 2−10 MBq/animal and 4−10 MBq per kg of body weight for larger animals for static imaging (5−10 min data acquisition). For the shorter imaging timeframes, e.g., for dynamic data acquisition with 1−2 min frame duration, the dose should be increased accordingly. Doses larger than 45 MBq in small animals and ca. 45 MBq per 15−20 cm of body length in larger animals would enable shorter imaging sessions but may require data correction for counting efficacy.

For biopharmaceuticals (e.g., proteins), labeling with ^{124}I provides an extra advantage of estimating the tissue residence and metabolization kinetics in the same PET study.

Pharmacological PET imaging with ^{124}I will be especially beneficial for large and/or rare animal studies.

AUTHOR INFORMATION

Corresponding Author

*Massachusetts General Hospital, Bartlett Hall 500R, 55 Fruit Street, Boston, MA 02114. Phone: 617-967-4245 (cell). Fax: 617-371-4927. E-mail: papisov@helix.mgh.harvard.edu.

ACKNOWLEDGMENT

This work was supported in part by Shire HGT (Cambridge, MA), which also provided model proteins.

REFERENCES

(1) Jeavons, A. P.; Chandler, R. A.; Dettmar, C. A. R. A 3D HIDAC-PET camera with sub-millimeter resolution for imaging small animals. *IEEE Trans. Nucl. Sci.* **1999**, *46*, 468–473.

(2) Tai, Y. C.; Chatziioannou, A.; Siegel, S.; Young, J.; Newport, D.; Goble, R. N.; Nutt, R. E.; Cherry, S. R. Performance evaluation of the microPET P4: a PET system dedicated to animal imaging. *Phys. Med. Biol.* **2001**, *46*, 1845–1862.

(3) Tai, Y. C.; Ruangma, A.; Rowland, D.; Siegel, S.; Newport, D. F.; Chow, P. L.; Laforest, R. Performance evaluation of the microPET focus: a third generation microPET scanner dedicated to animal imaging. *J. Nucl. Med.* **2005**, *46*, 455–463.

(4) Kim, J. S.; Lee, J. S.; Im, K. C.; Kim, S. J.; Kim, S. Y.; Lee, D. S.; Moon, D. H. Performance measurement of the microPET focus 120 scanner. *J. Nucl. Med.* **2007**, *48*, 1527–1535.

(5) Huisman, M. C.; Reder, S.; Weber, A. W.; Ziegler, S. I.; Schwaiger, M. Performance evaluation of the Philips MOSAIC small animal PET scanner. *Eur. J. Nucl. Med. Mol. Imaging* **2007**, *34*, 532–540.

(6) Kemp, B. J.; Hruska, C. B.; McFarland, A. R.; Lenox, M. W.; Lowe, V. J. NEMA NU 2−2007 performance measurements of the Siemens Inveon preclinical small animal PET system. *Phys. Med. Biol.* **2009**, *54*, 2359–2376.

(7) Wang, Y.; Seidel, J.; Tsui, B. M.; Vaquero, J. J.; Pomper, M. G. Performance evaluation of the GE Healthcare eXplore VISTA dual-ring small-animal PET scanner. *J. Nucl. Med.* **2006**, *47*, 1891–1900.

(8) Gregory, R. A.; Hooker, C. A.; Partridge, M.; Flux, G. D. Optimization and assessment of quantitative 124-I imaging on a Philips Gemini dual GS PET/CT system. *Eur. J. Nucl. Med. Mol. Imaging* **2009**, *36*, 1037–1048.

(9) Herzog, H.; Tellmann, L.; Qaim, S. M.; Spellerberg, S.; Schmid, A.; Coenen, H. H. PET quantitation and imaging of the non-pure positron-emitter iodine isotope 124I. *Appl. Radiat. Isot.* **2002**, *56*, 673–679.

(10) Vandenberghe, S. Three-dimensional positron emission tomography imaging with 124I and 86Y. *Nucl. Med. Commun.* **2006**, *27*, 237–245.

(11) Robinson, S.; Julyan, P. J.; Hastings, D. L.; Zweit, J. Performance of a block detector PET scanner in imaging non-pure positron emitters-modelling and experimental validation with 124I. *Phys. Med. Biol.* **2004**, *49*, 5505–5528.

(12) Pentlow, K. S.; Graham, M. C.; Lambrecht, R. M.; Cheung, N.-K. V.; Larson, S. M. Quantitative imaging of I-124 using positron emission tomography with applications to radioimmunodiagnosis and radioimmunotherapy. *Med. Phys.* **1991**, *18*, 357–366.

(13) Pentlow, K. S.; Graham, M. C.; Lambrecht, R. M.; Daghighian, F.; Bacharach, S. L.; Bendriem, B.; Finn, R. D.; Jordan, K.; Kalaigian, H.; Karp, J. S.; Robeson, W. R.; Larson, S. M. Quantitative imaging of Iodine-124 with PET. *J. Nucl. Med.* **1996**, *37*, 1557–1562.

(14) Herzog, H.; Tellmann, L.; Scholten, B.; Coenen, H. H.; Qaim, S. M. PET imaging problems with the non-standard positron emitters Yttrium-86 and Iodine-124. *Q. J. Nucl. Med. Mol. Imaging* **2008**, *52*, 159–165.

(15) Defrise, M.; Kinahan, P. E.; Townsend, D. W.; Michel, C.; Sibomana, M.; Newport, D. F. Exact and approximate rebinning algorithms for 3-D PET data. *IEEE Trans. Med. Imaging* **1997**, *16*, 145–158.

(16) Hudson, H. M.; Larkin, R. S. Accelerated image reconstruction using ordered subsets of projection data. *IEEE Trans. Med. Imaging* **1994**, *13*, 601–609.

(17) Qi, J.; Leahy, R. M.; Cherry, S. R.; Chatziioannou, A.; Farquhar, T. H. High-resolution 3D Bayesian image reconstruction using the microPET small-animal scanner. *Phys. Med. Biol.* **1998**, *43*, 1001–1013.

(18) Levin, C. S.; Hoffman, E. J. Calculation of positron range and its effect on the fundamental limit of positron emission tomography system spatial resolution. *Phys. Med. Biol.* **1999**, *44*, 781–799.

(19) Cherry, S. R.; Sorenson, J. A.; Phelps, M. E. *Physics in Nuclear Medicine*; Saunders/Elsevier Science: Philadelphia, PA, 2003.

(20) Strother, S. C.; Casey, M. E.; Hoffman, E. J. Measuring PET scanner sensitivity: relating countrates to image signal-to-noise ratios using noise equivalent counts. *IEEE Trans. Nucl. Sci.* **1990**, *37*, 783–788.

(21) Watson, C. C.; Newport, D.; Casey, M. E. A single scatter simulation technique for scatter correction in 3D PET. In *Three-Dimensional Image Reconstruction in Radiology and Nuclear Medicine*; Grangeat, P., Amans, J.-L., Eds.; Kluwer Academic Publishers: The Netherlands; 1996; pp 255−268.

(22) Watson, C. C. New faster image-based scatter correction for 3D PET. *IEEE Trans. Nucl. Sci.* **2000**, *47*, 1587–1594.

(23) Casey, M. E.; Gadagkar, H.; Newport, D. A component based method for normalization in volume PET. In *Proc. Intl. Meeting on Fully Three-Dimensional Image Reconstruction in Radiology and Nuclear Medicine*, Aix-les-Bains, France; 1995, pp 67−71.

(24) Loening, A. M.; Gambhir, S. S. AMIDE: a free software tool for multimodality medical image analysis. *Mol. Imaging* **2003**, *2*, 131–137.

(25) Visser, E. P.; Disselhorst, J. A.; Brom, M.; Laverman, P.; Gotthardt, M.; Oyen, W. J. G.; Boerman, O. C. Spatial resolution and sensitivity of the Inveon small-animal PET scanner. *J. Nucl. Med.* **2009**, *50*, 139–147.

(26) Matej, S.; Karp, J. S.; Lewitt, R. M.; Becher, A. J. Performance of the Fourier rebinning algorithm for PET with large acceptance angles. *Phys. Med. Biol.* **1998**, *43*, 787–795.

(27) Papisov, M. I.; Savelyev, V. Y.; Sergienko, V. B.; Torchilin, V. P. Magnetic drug targeting (I) In vivo kinetics of radiolabeled magnetic drug carriers. *Int. J. Pharm.* **1987**, *40*, 201–206.

(28) Papisov, M. I. Modeling in vivo transfer of long-circulating polymers (two classes of long circulating polymers and factors affecting their transfer in vivo). *Adv. Drug Delivery Rev.* **1995**, *16*, 127–137.

(29) Guggenheim, E. A. On the determination of the velocity constant of a unimolecular reaction. *Philos. Mag. (series 7)* **1926**, *2*, 538−543.

(30) Daube-Witherspoon, M. E.; Karp, J. S.; Casey, M. E.; DiFilippo, F. P.; Hines, H.; Muehllehner, G.; Simcic, V.; Stearns, C. W.; Adam, L. E; Kohlmyer, S.; Sossi, V. PET performance measurements using the NEMA NU 2-2001 standard. *J. Nucl. Med.* **2002**, *43*, 1398–1409.

(31) Friedman, J. E.; Watson, J. A., Jr.; Lam, D. W.-H.; Rokita, S. E. Iodotyrosine Deiodinase Is the First Mammalian Member of the NADH Oxidase/Flavin Reductase Superfamily. *J. Biol. Chem.* **2006**, *281*, 2812–2819.

(32) Ullberg, S.; Ewaldsson, B. Distribution of radio-iodine studied by whole-body autoradiography. *Acta Radiol.: Ther., Phys., Biol.* **1964**, *2*, 24–32.

(33) Hays, M. T.; Solomom, D. H. Influence of the gastrointestinal iodide cycle on the early distribution of radioactive Iodide in man. *J. Clin. Invest* **1965**, *44*, 117–27.

(34) Vallabhajosula, S. Radiopharmaceuticals for PET. In *Clinical Nuclear Medicine*; Biersack, H.-J., Freeman, L. M., Eds.; Springer-Verlag: Berlin, Heidelberg, New York, 2007; pp 50−76.